



LAWRENCE
LIVERMORE
NATIONAL
LABORATORY

LLNL-JRNL-780397

Effect of laser power on roughness and porosity in laser powder bed fusion stainless steel 316L alloys measured by X-ray tomography

Jean-Baptiste Forien, Philip J. DePond, Gabe M. Guss, Bradley H. Jared, Jonathan D. Madison, Manyalibo J. Matthews

August 2019

International Journal of Materials Research

Jean-Baptiste Forien^a, Philip J. DePond^a, Gabe M. Guss^b, Bradley H. Jared^c, Jonathan D. Madison^c, Manyalibo J. Matthews^a

^a *Physical and Life Sciences Directorate, Lawrence Livermore National Laboratory, Livermore CA USA*

^b *Engineering Directorate, Lawrence Livermore National Laboratory, Livermore CA USA*

^c *Material, Physical and Chemical Sciences Center, Sandia National Laboratories, Albuquerque, NM USA*

Effect of laser power on roughness and porosity in laser powder bed fusion stainless steel 316L alloys measured by X-ray tomography

The quality of metal objects fabricated via laser powder bed fusion are highly affected by process parameters, and their influence on final products is yet to be fully explored. In this work, pyrometry signals of the melt pool were collected from a set of stainless-steel samples during manufacturing and the effect of laser power on porosity and roughness of final printed parts was analyzed. Results show that the melt pool pyrometry signal of contours increases with higher laser power, whereas it is lower and decreases for the infilled part. Post-built X-ray computed tomography imaging reveals that porosity decreases while sample roughness increases upon increasing laser power. The decrease in porosity with increasing laser power is attributed to the larger size of the contour welds that were printed first, leading to an increase in dimension of the final products.

Keywords: Laser powder bed fusion; Porosity; Roughness; X-ray tomography; Pyrometry

1. Introduction

Laser powder bed fusion (LPBF) is a relatively recent metal additive manufacturing (AM) process capable of building 3D objects layer by layer using a selectively scanned, high power laser beam. This technique offers the possibility to build complex geometries based on a digital file, with tailored material properties for specific applications [1, 2] and with minimal waste [3, 4].

However, the LPBF process generates voids and pores which are known to act as stress concentrators under loading and can lead to component failure [5]. Several types of voids can appear during printing [6, 7] ranging in size up to several hundred microns. Lack of fusion voids are typically caused through lack of energy deposited on the powder that does not allow metallic particles to fully melt and consolidate. These defects are more likely to be irregular or elongated and are present between successive build layers [8–10]. One particularly troublesome class of lack of fusion voids is due to trapped spatter particles which originate from material ejecta expelled out of the vicinity of the melt pool and landing on the build regions [11, 12]. Another type of voids named end-of-track defects are created when the laser reaches the end of its course in so-called ‘sky writing’ mode or does an abrupt path change that disturbs the steady state melt pool shape [13]. Voids also appear in the form of keyhole pores, which are generated in keyhole-mode melting when the local energy density is too high due to changes in scan velocity, spikes in absorbed laser energy, or changes in local thermal boundary conditions. These situations cause a vapor depression in the melt pool to expand and emit gas bubbles that become entrapped in the weld [14–16]. Porosity can also be associated with pores inside the powder itself, created during the atomization process of most commercial powders [17].

Different aspects of pore creation produced during laser powder bed fusion have been investigated by X-ray computed tomography (CT) and reported in several studies. Observation of porosity with X-ray CT in stainless steel 316L samples printed via LPBF revealed that the number, shape, and location of pores vary according to the sample build orientation [18]. Similarly, it was noted via X-ray CT that vertical defects are preferentially oriented along the build direction and that tall induced pores, up to 180 μm in the study, are partially resorbed when subsequent layers of powder are sintered [19]. Kasperovich et al. [20] investigated the effect of processing

parameters on pore formation produced by LPBF in Ti-6Al-4V (Ti64) alloys by X-ray tomography and showed that both pore size and shape vary with the amount of energy deposited onto the build plate. The authors also found lack of fusion type pores appearing at insufficient energy density are elongated and narrow, and preferentially oriented perpendicularly to the build direction. However, pores are spherical with diameter higher than 50 μm at excessive energy density, presumably created by the keyhole effect. It was also found that the number of pores is mainly governed by the power and velocity of laser [20, 21]. Tomography comparisons of pores created in contour and infill hatching region were measured in selective electron beam melting [22]. Results showed that a large number of spherical pores appear to be concentrated in the infill hatched region whereas a lower number of irregular shaped pores attributed to lack of fusion are found in contour region. Powder feedstock porosity of titanium, aluminum and magnesium was also studied using tomography and it was demonstrated that X-ray CT yields comparable results to standard characterization methods such as pycnometry and metallography [23]. Roughness and surface finish measurements were performed on different types of AM metal using X-ray tomography. In a study of porous titanium structures, tomography surface roughness measurements done before and after cleaning of the struts could not conclude on the possible positive effect of the cleaning procedure due to high standard deviation and no statistical difference [24]. In another study on nickel alloy 625 and 17-4 stainless steel [25], the authors show that a resolution of $\sim 10 \mu\text{m}/\text{pixel}$ prevents strong quantitative analysis of the surface or relevant comparison to the laser confocal microscope surface data. In a comparison of X-ray CT with standard roughness measurement techniques [26], the authors concluded that X-ray tomography yields similar results to standard profile measuring systems for surface with micro-scale roughness, whereas spatial resolution and noise level in images are limiting factors and prevent the use of tomography for smooth roughness surface measurements. Deformation and failure mechanisms of 316L stainless steel samples produced via LPBF were studied using in-situ tensile testing combined with X-ray tomography [27]. Results show that low porosity samples behave similarly to wrought samples, whereas high porosity samples with heterogeneous pore distributions have inferior mechanical properties and display flaw driven types of failure.

Post-build inspection such as CT or laser confocal microscopy is required to investigate porosity and surface roughness to make sure the printed parts are defect-free or manufactured according to the specifications. While these inspections can take time and are complicated in the case of large parts, alternative measurements such as process monitoring are being developed to enable the detection of defects [7, 28]. One of the methods consists of measuring the temperature at the surface of the melt pool using pyrometry. Usage of this technique for high-speed, high-resolution real-time temperature measurement in different types of laser welding has been demonstrated in several studies [29, 30]. Correlation of laser parameters on pyrometry signal was investigated for powder thickness [31, 32], hatch distance [31] and laser power [33, 34].

In this work, a series of dog-bone samples were printed with different laser power and the relative melt pool temperature signal was measured during printing (Fig. 1a). The effect of laser power on porosity and surface roughness was then quantified by X-ray computed tomography (Fig. 1b).

2. Experimental procedure

2.1. Materials, printing parameters

Gas atomized 316L stainless steel powder manufactured by Additive Metal Alloys Ltd., Holland, OH, USA was used in this study. The powder had a concentration in wt.% of 16.5 Cr, 69.5 Fe, 1.27 Mn, 2.02 Mo and 10.4 Ni for its major constituents. The powder was sieved to contain particles with size ranging from 15 to 45 μm . Powder was successively deposited on a substrate to form a 50 μm thick layer. An open architecture LPBF machine (Aconity3D, Aachen, Germany) equipped with a 400 W continuous wave fiber laser was used to melt the powder at specific locations under argon atmosphere with a beam size of about 100 μm . Beam profiles may have been larger and distorted due to thermal lensing discovered after these experiments. Dog-bone-shaped samples with 5 x 1 x 1 mm^3 (length x width x thickness) gauge section were printed with their long axis along the building direction. Within each layer, the sample contour was printed first, followed by a 45-degree zig-zag pattern scan strategy. The hatching pattern was rotated by 90 degrees for each layer with a hatching distance of 100 μm and the laser power was reduced to its minimum at turn arounds. Table 1 shows the laser scan parameters used in this study.

2.2. High-speed pyrometry

Figure 1 shows a simplified schematic of the pyrometer configuration used in this study. Thermal emission from the melt pool is collected through the scan mirrors and imaging optics used to focus the laser source. A dichroic optic reflects ~ 1070 nm long-pass filtered light while passing 1500–1700 nm light band. The remaining long-passed light is then directed to a coaxially-aligned, fiber-coupled InGaAs-based optical pyrometer operating at 100 kHz. The input of a 200 μm core multimode fiber was 1:1 imaged onto the melt pool, thus limiting the collection area to a circular window of 200 μm diameter with the laser focus approximately at the center. Additional description of the experimental setup can be found in DePond et al. [35] and Yuan et al. [36]. Values of pyrometry signals are given in arbitrary units since true temperature measurements of the melt pool using single color pyrometry leads to incorrect values due to unknown emissivity of the hot surface and its possible variation in the course of measurements [37].

2.3. X-ray computed tomography

Cone beam micro-computed tomography was performed at Sandia National Laboratories using a micro-CT system (North Star imaging Inc., Rogers, USA) with a table-mounted X-ray source (XRAYWorX[®], Garbsen, Germany) placed ~ 20 mm away from the sample and with a tube voltage of 220 kV (285 μA). A Cu pre-filter at the X-ray source having a thickness of 0.3 mm was used to optimize inspection and a magnification factor of 12.51x was used resulting in a cubic voxel size of 10.2 μm /voxel edge. For each scan, 1599 projections were obtained with 16 frames averaging over a data collection interval of 3 hours and 12 minutes per sample. Images were collected using a flat-panel detector (Varian model 2520DX, Salt Lake City, USA) equipped with direct deposit cesium iodide conversion screen and pixel pitch of 127 μm^2 . Data from the collected projections were initially reconstructed using VGStudio Max software (Volume Graphics, Heidelberg, Germany) and then exported as .tif stacks in each of the primary orthogonal directions at the resolution of the dataset.

2.3. Image processing and analysis

Characterization of porosity and surface roughness was performed on the neck section of dog-bone samples. The same length of section (4.3 mm) was considered for the samples and subdivided into 5 equal sub-volumes (5 x 0.86 mm) for statistical purposes. Data processing and

visualization were performed using Fiji (NIH, USA, V 1.52e) [38] with BoneJ [39], MorpholibJ [40] and volume viewer plugins. Extraction of pore information was performed on the 8-bit reconstructed volume samples as shown in Fig. 2. A mask of each sample was obtained by applying a 2D mean filter with a 2-pixel radius followed by an automatic thresholding using a mean algorithm. Volume corresponding to samples was extracted and 3D filled for holes. The resulting binary volumes were used in an AND operation with the original stacks and converted to 32-bit images to obtain reconstructed volume of samples only. Normalization of these stacks with its 2D mean filtered (5-pixel radius) duplicate were further 2D mean filtered (2-pixel radius) and binarized using mean algorithm. The volumes were morphologically 3D dilated and eroded to discard single voxel artifacts. Finally, pores were labelled after extracting largest volumes and binary inversion steps.

Surface roughness characterization was performed by extracting the surface of the binarized volume obtained in the same way as for porosity analysis. Regions of interest of $1 \times 4.3 \text{ mm}^2$ (length x width) were considered in the middle of neck sections of both sides of the samples and further fitted using a 1st order polynomial surface curve. Results of the fitted surface were subtracted from the surface and the root mean square average was obtained by considering the square root of the sum of the squares of the individual heights and depths of 5 sub-sections of equal size (Fig. 3).

3. Results and discussion

The effect of laser power on porosity was investigated in the neck section of the dog-bone samples. Volume distributions of pores for the different samples are shown Fig. 4. The results indicate that the mean closest neighbor distance between pores is constant with a value of $127 \pm 4 \text{ }\mu\text{m}$ for laser power ranging from 310 to 340 W and then gradually increases to $152 \pm 9 \text{ }\mu\text{m}$ for laser power ranging from 350 to 380 W (Fig. 5a). Note that the increase of the mean value indicates a bigger distance between pores and that the increase in standard deviation can be interpreted as a decrease in uniformity of pore distribution. The rate of decrease in porosity with increasing laser power from 310 to 330 W is initially slow (1.32 to 1.26 %). Upon further increase in laser power to 382 W, a drastic decrease in porosity (1.19 to 0.74 %) as in Fig. 5b was observed.

However, the number of pores per millimeter of notched section ($\sim 124 \pm 14$) and the mean pore diameter ($\sim 55.3 \pm 1.8 \mu\text{m}$) remain constant with laser power (Fig. 5c and d). The cross-sectional area at the neck sections remain stable at $1.83 \times 10^6 \pm 1.1 \times 10^5 \mu\text{m}^3$ with laser power ranging from 310 to 340 W and increases with laser power up to $2.9 \times 10^6 \pm 1.1 \times 10^5 \mu\text{m}^3$ when laser power of 382 W is used (Fig. 5e). Histograms of pore volume distribution shown in Fig. 5f indicate an exponential decrease of the number in small pores compared to the number of bigger pores for all samples.

It can be concluded from Fig. 5 that the decrease in porosity can only arise from the increase in cross-sectional area as both mean diameter and number of pores remain stable with increasing laser power. In addition, no lack-of-fusion type of pores were found in the samples as the laser power is increased. It should be noted that the scan path and commanded geometry of all samples were the same. Decrease in porosity with increasing laser power was also found for Ti64 alloy samples produced by laser powder bed fusion [8, 20]. In each of these studies, a wide range of laser powers was applied resulting in the creation of lack of fusion pores at low energy to more spherical pores associated with keyholes at excessive energy. Using a wide range of laser powers, Kasperovich et al. [16] observed an increase in porosity above a certain threshold of applied energy, enabling them to determine a region of laser power that yielded minimal defects.

Three-dimensional surface plots of the roughness at the neck section of the samples are shown in Fig. 6a. Quantitative analysis of the root mean squared reveals that surface roughness increases with laser power on both sides of the samples from $\sim 3.4 \pm 0.5$ to $\sim 6.6 \pm 1.1$ rms for side 1 and from $\sim 2.8 \pm 0.4$ to $\sim 6.2 \pm 0.7$ rms for side 2 for 310 and 382 W laser powers respectively (Fig. 6b). The 45 degree scan strategy adopted to print these samples resulted in the hatch starting in one corner and finished in the opposite corner. Between layers the start corner was moved, but all start corners were on one of the flat sides of the dog-bone samples and the end corners were on the other side (Fig. 1a). We observed a systematic line of defects at the end corner, which is presumably a result of overheating due to hatching with successive short scan vectors. The difference in roughness of the sides could therefore be attributed to this scan strategy. Although it was suggested that quantitative analysis of roughness measurements is difficult at a resolution

of $\sim 10 \mu\text{m}/\text{voxel}$ [25], it is possible to see a clear increase in roughness with increasing laser power in this study.

Pyrometry analysis indicates that the average pyrometry signal increases with laser power when considering the contour only, whereas it decreases when considering an average of hatching as shown in Fig. 7. The increase in melt pool temperatures of the contour with laser power was also determined using pyrometry in single track laser welding experiments [41]. In addition, an increase in melt pool temperature was found to be correlated with an increase in melt pool size [42–44], which explains the increase in the size of the samples. The higher pyrometry values of contours versus infills can be attributed to either the fact that laser power was null at the turn around or the fact that contours were printed first. In the second hypothesis, which was also reported by Craeghs et al. [45], the melt pool temperature is heat insulated and the heat flux is directed toward the substrate. Whereas, when the subsequent infill is printed, the heat flux of the temperature is directed both towards the substrate and the already solidified material from the contour. The decrease in melt pool temperature of the filling with increasing power is attributed to this effect too. At higher powers, the weld track is wider leading to contour welds that cover more of the overall welded region. As a result, less and less powder remains to weld causing the decrease in pyrometry signal with increasing laser power.

4. Conclusions

X-ray tomography of dog-bone samples prepared using laser powder bed fusion allowed us to determine the effect of laser power on porosity and surface roughness. Results show a decrease in porosity and an increase in sample volume and surface roughness with higher laser power, that we ascribe to the adopted scan strategy. Indeed, scan strategy plays an important role in the quality of the final build by having influence on the residual stress [46–48], surface roughness [49, 50] and defect population [9, 46]. In our case, contours were printed first and the pyrometry signal of the contour indicates that temperature at the surface of the melt pool increases with laser power. Since melt pool temperature and width are intimately correlated the contour track ended up being broader, explaining the increase in volume and roughness of printed samples at high laser power. At the same time, the range of laser powers used in this study did not affect the

porosity and number of voids created in the infill region of the sample. Thus, the decrease in porosity with higher laser power is mainly attributed to the increase in sample volume with increased laser power.

Ideally, tomography and pyrometry 3D-data could be spatially overlaid onto each other to possibly obtain correlation between melt pool temperature and the presence of pores. However, pores created in a layer have a high chance of disappearing with subsequent layers [19], making the recorded pyrometry signal not representative of the end state of the printed sample and the correlation of the two datasets challenging to accomplish. Future studies could use a dynamic treatment approach of pyrometry data to obtain a more realistic representation of the melt pool temperature or heat accumulation of the object after the print and make the correlation to tomography and detection of defects easier.

This work was performed under the auspices of the U.S. Department of Energy by Lawrence Livermore National Laboratory under Contract DE-AC52-07NA27344, supported by the Office of Laboratory Directed Research and Development (LDRD), tracking numbers 15-ERD-037 and 18-SI-003. Sandia National Laboratories is a multi-mission laboratory managed and operated by National Technology & Engineering Solutions of Sandia, LLC, a wholly owned subsidiary of Honeywell International Inc., for the U.S. Department of Energy's National Nuclear Security Administration under contract DE-NA0003525. The authors would also like to thank Carl Jacques, Kyle Thompson, Burke Kernen and David Moore for micro-computed tomography experiments at Sandia.

References:

- [1] J.A. Koepf, M.R. Gotterbarm, M. Markl, C. Körner: *Acta Mater.* 152 (2018) 119–126. DOI:10.1016/j.actamat.2018.04.030
- [2] Y.P. Yang, M. Jamshidinia, P. Boulware, S.M. Kelly: *Comput. Mech.* 61 (2018) 599–615. DOI:10.1007/s00466-017-1528-7
- [3] S.H. Huang, P. Liu, A. Mokasdar, L. Hou: *Int. J. Adv. Manuf. Technol.* 67 (2013) 1191–1203. DOI:10.1007/s00170-012-4558-5
- [4] L.E. Murr, S.M. Gaytan, D.A. Ramirez, E. Martinez, J. Hernandez, K.N. Amato, P.W. Shindo, F.R. Medina, R.B. Wicker: *J. Mater. Sci. Technol.* 28 (2012) 1–14. DOI:10.1016/S1005-0302(12)60016-4
- [5] B. Zhang, Y. Li, Q. Bai: *Chin. J. Mech. Eng.* (2017) 1–13. DOI:10.1007/s10033-017-0121-5.

- [6] N.T. Aboulkhair, N.M. Everitt, I. Ashcroft, C. Tuck: *Addit. Manuf.* 1–4 (2014) 77–86. DOI:10.1016/j.addma.2014.08.001
- [7] M. Grasso, B.M. Colosimo: *Meas. Sci. Technol.* 28 (2017) 044005. DOI:10.1088/1361-6501/aa5c4f
- [8] R. Cunningham, S.P. Narra, C. Montgomery, J. Beuth, A.D. Rollett: *JOM.* 69 (2017) 479–484. DOI:10.1007/s11837-016-2234-1
- [9] S. Tamas-Williams, H. Zhao, F. Léonard, F. Derguti, I. Todd, P.B. Prangnell: *Mater. Charact.* 102 (2015) 47–61. DOI:10.1016/j.matchar.2015.02.008
- [10] X. Zhou, D. Wang, X. Liu, D. Zhang, S. Qu, J. Ma, G. London, Z. Shen, W. Liu: *Acta Mater.* 98 (2015) 1–16. DOI:10.1016/j.actamat.2015.07.014
- [11] S. Ly, A.M. Rubenchik, S.A. Khairallah, G. Guss, M.J. Matthews: *Sci. Rep.* 7 (2017) 4085. DOI:10.1038/s41598-017-04237-z
- [12] M. Simonelli, C. Tuck, N.T. Aboulkhair, I. Maskery, I. Ashcroft, R.D. Wildman, R. Hague: *Metall. Mater. Trans. A.* 46 (2015) 3842–3851. DOI:10.1007/s11661-015-2882-8
- [13] A.M. Mancisidor, F. Garciandia, M.S. Sebastian, P. Álvarez, J. Díaz, I. Unanue: *Phys. Procedia.* 83 (2016) 864–873. DOI:10.1016/j.phpro.2016.08.090
- [14] N.P. Calta, J. Wang, A.M. Kiss, A.A. Martin, P.J. Depond, G.M. Guss, V. Thampy, A.Y. Fong, J.N. Weker, K.H. Stone, C.J. Tassone, M.J. Kramer, M.F. Toney, A. Van Buuren, M.J. Matthews: *Rev. Sci. Instrum.* 89 (2018) 055101. DOI:10.1063/1.5017236
- [15] C.L.A. Leung, S. Marussi, R.C. Atwood, M. Towrie, P.J. Withers, P.D. Lee: *Nat. Commun.* 9 (2018) 1355. DOI:10.1038/s41467-018-03734-7
- [16] C.L.A. Leung, S. Marussi, M. Towrie, J. del Val Garcia, R.C. Atwood, A.J. Bodey, J.R. Jones, P.J. Withers, P.D. Lee: *Addit. Manuf.* 24 (2018) 647–657. DOI:10.1016/j.addma.2018.08.025
- [17] M. Iebba, A. Astarita, D. Mistretta, I. Colonna, M. Liberini, F. Scherillo, C. Pirozzi, R. Borrelli, S. Franchitti, A. Squillace: *J. Mater. Eng. Perform.* 26 (2017) 4138–4147
- [18] G. Ziółkowski, E. Chlebus, P. Szymczyk, J. Kurzac: *Arch. Civ. Mech. Eng.* 14 (2014) 608–614. DOI:10.1016/j.acme.2014.02.003
- [19] A. du Plessis, S.G. le Roux, G. Booysen, J. Els: *3D Print. Addit. Manuf.* 3 (2016) 48–55. DOI:10.1089/3dp.2015.0034
- [20] G. Kasperovich, J. Haubrich, J. Gussone, G. Requena: *Mater. Des.* 105 (2016) 160–170. DOI:10.1016/j.matdes.2016.05.070
- [21] F. Imani, M. Montazeri, H. Yang, A. Gaikwad, P. Rao, E. Reutzel: *Proc. ASME 2018 13th Int. Manuf. Sci. Eng. Conf.*, ASME, College Station, TX, (2018).
- [22] F. Leonard, S. Tamas-Williams, I. Todd: *Proc. 6th Conf. Ind. Comput. Tomogr.*, Wels, Austria, (2016).
- [23] K. Heim, F. Bernier, R. Pelletier, L.-P. Lefebvre: *Case Stud. Nondestruct. Test. Eval.* 6, Part A (2016) 45–52. DOI:10.1016/j.csndt.2016.09.002
- [24] T.B. Kim, S. Yue, Z. Zhang, E. Jones, J.R. Jones, P.D. Lee: *J. Mater. Process. Technol.* 214 (2014) 2706–2715. DOI:10.1016/j.jmatprotec.2014.05.006
- [25] J.C. Fox, F.H. Kim, Z.C. Reese, C. Evans: *Proc. Euspen/ASPE Conf. Dimens. Accuracy Surf. Finish Addit. Manuf.*, Leuven, Be (2017).
- [26] G. Kerckhofs, G. Pyka, M. Moesen, S.V. Bael, J. Schrooten, M. Wevers: *Adv. Eng. Mater.* 15 (2013) 153–158. DOI:10.1002/adem.201200156

- [27] H.D. Carlton, A. Haboub, G.F. Gallegos, D.Y. Parkinson, A.A. MacDowell: *Mater. Sci. Eng. A* 651 (2016) 406–414. DOI:10.1016/j.msea.2015.10.073
- [28] Z.Y. Chua, I.H. Ahn, S.K. Moon: *Int. J. Precis. Eng. Manuf.-Green Technol.* 4 (2017) 235–245. DOI:10.1007/s40684-017-0029-7
- [29] M. Ignatiev, I. Smurov, G. Flamant: *Meas. Sci. Technol.* 5 (1994) 563. DOI:10.1088/0957-0233/5/5/016
- [30] F. Bayle, M. Doubenskaia: *Proc Fundam. Laser Assist. Micro- Nanotechnologies*, 2008: pp. 698505-698505–8. DOI:10.1117/12.786940
- [31] M. Pavlov, M. Doubenskaia, I. Smurov: *Phys. Procedia.* 5 (2010) 523–531. DOI:10.1016/j.phpro.2010.08.080
- [32] M. Doubenskaia, M. Pavlov, Y. Chivel: *Key Eng. Mater.* 431 (2010) 458–461. DOI:10.4028/www.scientific.net/KEM.437.458
- [33] A. Lehti, L. Taimisto, H. Piili, O. Nyrhilä, A. Salminen: *ICALEO* (2011).
- [34] Y. Chivel, I. Smurov: *Phys. Procedia.* 5 (2010) 515–521. DOI:10.1016/j.phpro.2010.08.079.
- [35] P.J. DePond, G. Guss, S. Ly, N.P. Calta, D. Deane, S. Khairallah, M.J. Matthews: *Mater. Des.* 154 (2018) 347–359. DOI:10.1016/j.matdes.2018.05.050
- [36] B. Yuan, G.M. Guss, A.C. Wilson, S.P. Hau-Riege, P.J. DePond, S. McMains, M.J. Matthews, B. Giera: *Adv. Mater. Technol.* 3 (2018) 1800136. DOI:10.1002/admt.201800136
- [37] M. Doubenskaia, P. Bertrand, I. Smurov: *Surf. Coat. Technol.* 201 (2006) 1955–1961. DOI:10.1016/j.surfcoat.2006.04.060
- [38] J. Schindelin, I. Arganda-Carreras, E. Frise, V. Kaynig, M. Longair, T. Pietzsch, S. Preibisch, C. Rueden, S. Saalfeld, B. Schmid, J.-Y. Tinevez, D.J. White, V. Hartenstein, K. Eliceiri, P. Tomancak, A. Cardona: *Nat. Methods.* 9 (2012) 676–682. DOI:10.1038/nmeth.2019
- [39] M. Doube, M.M. Kłosowski, I. Arganda-Carreras, F.P. Cordelières, R.P. Dougherty, J.S. Jackson, B. Schmid, J.R. Hutchinson, S.J. Shefelbine: *Bone.* 47 (2010) 1076–1079. DOI:10.1016/j.bone.2010.08.023
- [40] D. Legland, I. Arganda-Carreras, P. Andrey: *Bioinformatics.* 32 (2016) 3532–3534. DOI:10.1093/bioinformatics/btw413
- [41] I. Smurov: *Laser-Assist. Microtechnology 2000*, International Society for Optics and Photonics (2001).
- [42] I. Yadroitsev, P. Krakhmalev, I. Yadroitsava: *J. Alloys Compd.* 583 (2014) 404–409. DOI:10.1016/j.jallcom.2013.08.183
- [43] T. Craeghs, F. Bechmann, S. Berumen, J.-P. Kruth: *Phys. Procedia.* 5 (2010) 505–514. DOI:10.1016/j.phpro.2010.08.078
- [44] P. Norman, H. Engström, A.F.H. Kaplan: *J. Phys. Appl. Phys.* 41 (2008) 195502. DOI:10.1088/0022-3727/41/19/195502
- [45] T. Craeghs, S. Clijsters, E. Yasa, F. Bechmann, S. Berumen, J.-P. Kruth: *Opt. Lasers Eng.* 49 (2011) 1440–1446. DOI:10.1016/j.optlaseng.2011.06.016
- [46] H. Ali, H. Ghadbeigi, K. Mumtaz: *Mater. Sci. Eng. A.* 712 (2018) 175–187. DOI:10.1016/j.msea.2017.11.103
- [47] L. Parry, I.A. Ashcroft, R.D. Wildman: *Addit. Manuf.* 12 (2016) 1–15. DOI:10.1016/j.addma.2016.05.014
- [48] J. Robinson, I. Ashton, P. Fox, E. Jones, C. Sutcliffe: *Addit. Manuf.* 23 (2018) 13–24. DOI:10.1016/j.addma.2018.07.001

- [49] S. Ghouse, S. Babu, R.J. Van Arkel, K. Nai, P.A. Hooper, J.R.T. Jeffers: Mater. Des. 131 (2017) 498–508. DOI:10.1016/j.matdes.2017.06.041
- [50] P. Wang, W.J. Sin, M.L.S. Nai, J. Wei: Mater. Basel Switz. 10 (2017). DOI:10.3390/ma10101121

Correspondence address:

Jean-Baptiste Forien PhD
Physical and Life Sciences Directorate
Materials science division
Lawrence Livermore National Laboratory
7000 East Ave
Livermore CA 94550
USA
Tel: +1 925-422-2989
e-mail: forien1@llnl.gov

List of figure and table captions:

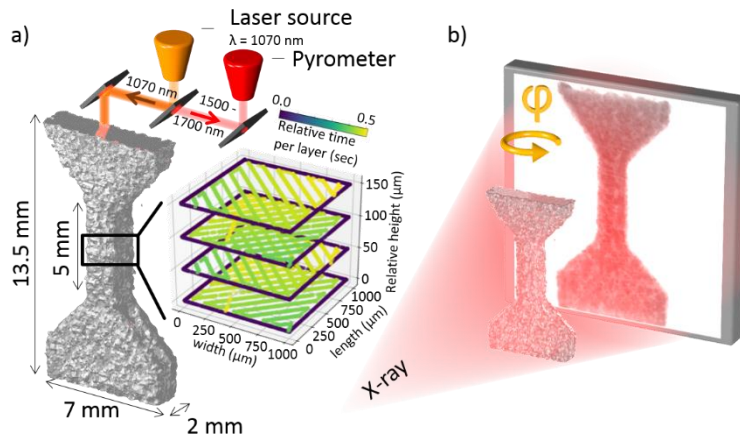


Figure 1: Schematic illustration of (a) laser powder bed fusion experiment with co-axial in-situ pyrometry monitoring and, (b) ex-situ x-ray tomography experiments. Each layer was printed with a contour scan first followed by a 45° hatching scan strategy. A rotation of 90° was used between each layer.

Table 1: Scanning parameters of the dog-bone samples with varying laser power.

Process parameters	Values
P – laser power (W)	310 – 320 – 330 – 340 – 350 – 360 – 370 – 382
v – scanning velocity ($\text{mm}\cdot\text{s}^{-1}$)	300
h – hatch distance (μm)	100
δ – layer thickness (μm)	50
Laser spot size (μm)	100

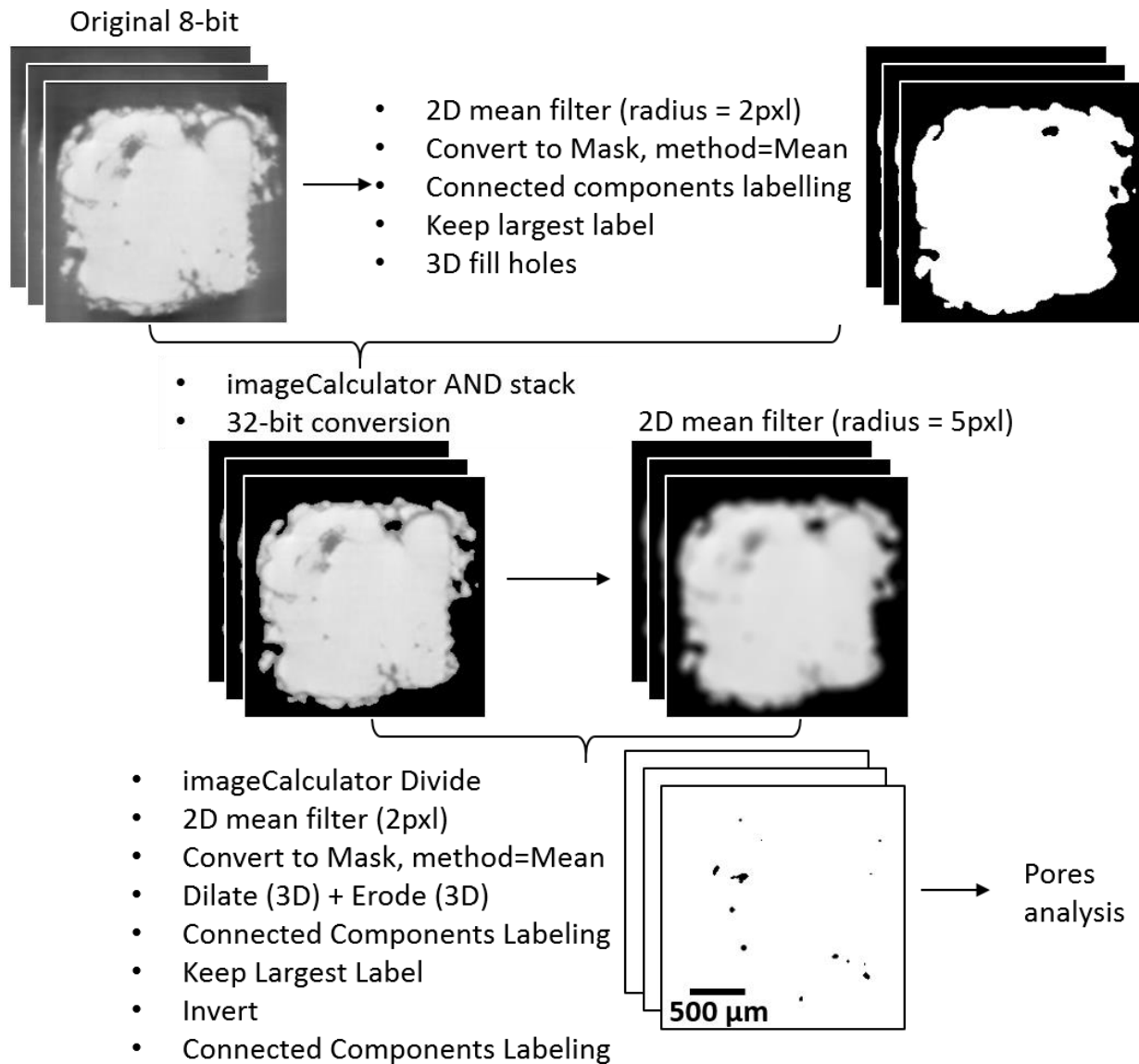


Figure 2: Flowchart of image processing path used to quantify pores from tomography reconstructions. Sample volumes were separated from background by applying a 2D mean filter with a 2-pixel radius on the original 8-bit reconstruction images and 3D filling holes function. The original volume was masked with the binarized data, converted to 32-bit and normalized with a 5-pixel radius 2D mean filtered copy of itself. The resulting volume was 2D filtered with 2-pixel radius and segmented using a mean method threshold. Three-dimensional dilate and erode steps were performed on the binarized data to remove the smallest objects. All image processing steps were performed using Fiji [38] with BoneJ [39] and MorphoLibJ [40] plugins.

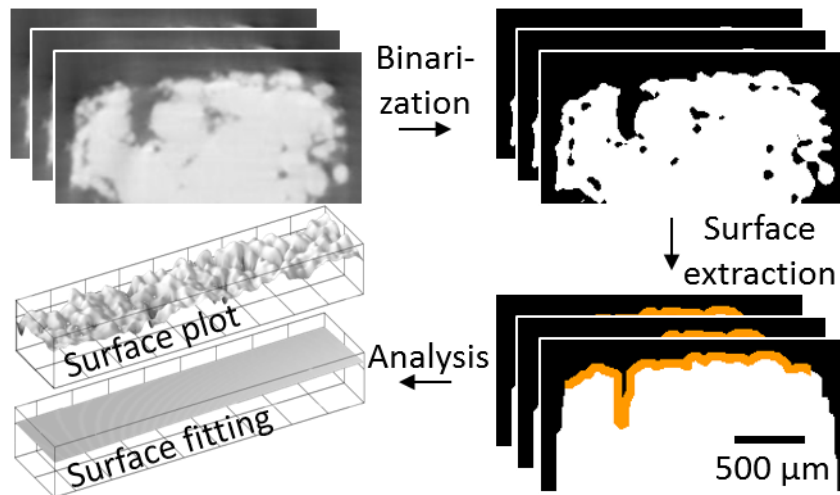


Figure 3: Flowchart of image processing path used to quantify surface roughness from tomography reconstructions. Binarized volumes were obtained using the same process as for the porosity analysis using a region of interest of $1 \times 4.3 \text{ mm}^2$ (width x length) taken in the middle gauge sections. Both sides of dog-bone samples were considered. First order polynomial fitted surfaces were subtracted from the gauge section surface and root mean square measurements were performed on five sub-sections of equal size by considering the square root of the sum of the squares of the individual heights and depths.

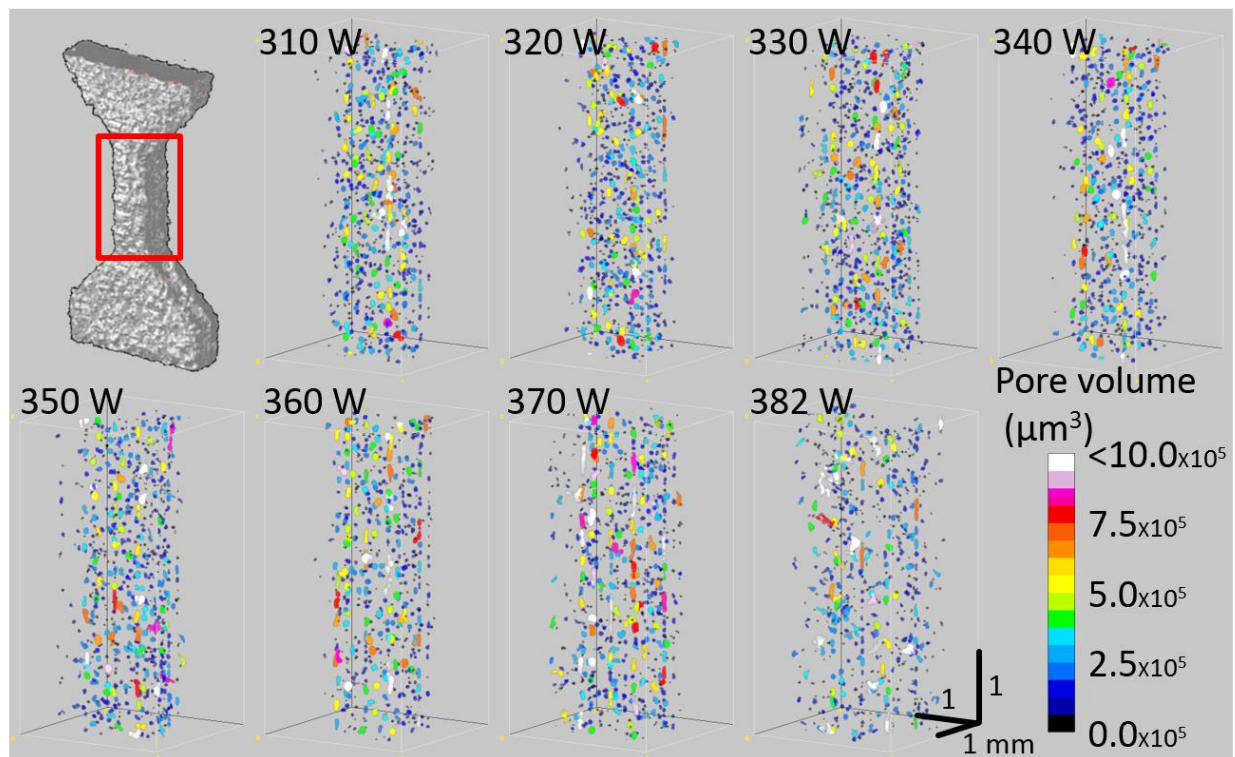


Figure 4: Distribution of pores at the neck section of each samples printed at different laser powers. Color bar corresponds to pore volume in μm^3 .

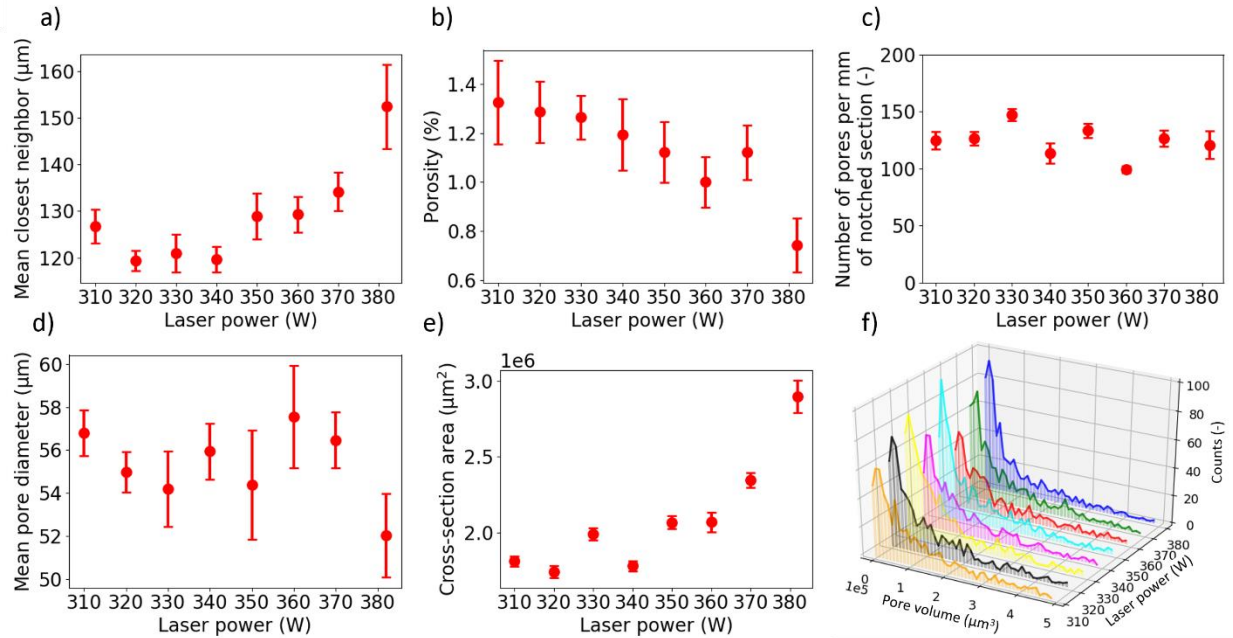


Figure 5: Results of the influence of laser power on pores at the neck section of the dog-bone samples. (a) mean closest distance between pores, (b) porosity, (c) number of pores per mm of notched section, (d) mean pore diameter, (e) cross-section area of AM metal part in neck section, and (f) pore volume distribution at different laser power. Error bars correspond to standard deviations.

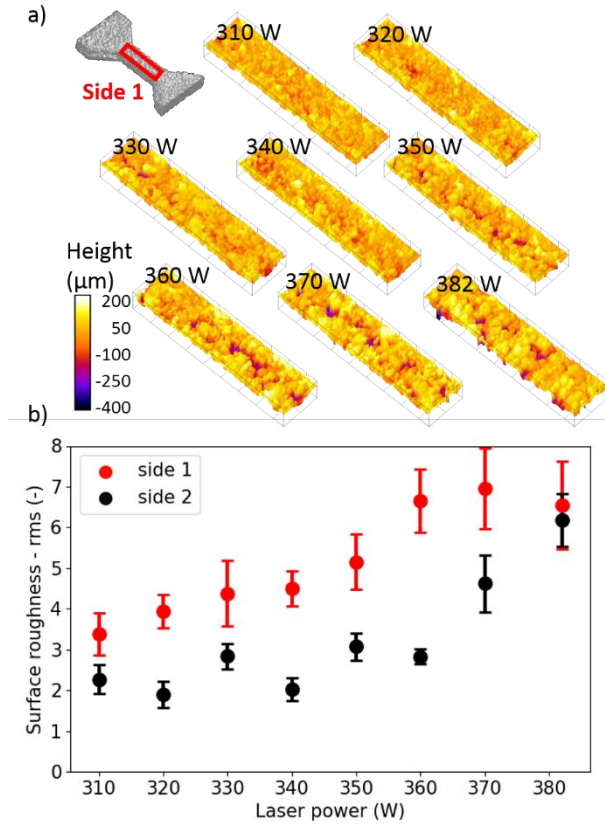


Figure 6: (a) Three-dimensional surface plots of one side of the gauge section of $1 \times 4.3 \text{ mm}^2$ (width x length) of the samples printed with varying laser power. Each map was subtracted by using its 1st order polynomial fit. Note, the increase in depth of the valley with increasing laser power. (b) Increasing root mean square surface roughness measurement of both side 1 and 2 of dog-bones samples with increasing laser power. Error bars correspond to standard deviations.

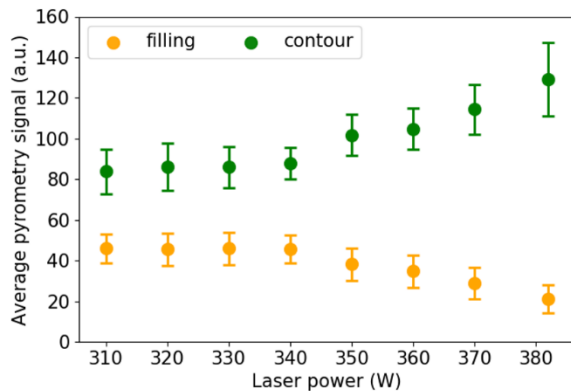


Figure 7: Results of the influence of laser power on pyrometry signal at the neck section for contour and infill hatching regions. Melt pool temperature of the contour hatching increases with laser power, whereas it decreases for infill hatching. Error bars correspond to standard deviations.